Magnetic domains in two distinct antiferromagnetic phases of CuO

R. Misawa,[1,*] K. Arakawa,[1] H. Ueda [iD],[2] H. Nakajima [iD],[3] S. Mori,[3] Y. Tanaka,[4] and T. Kimura [iD][1]

[1]*Department of Advanced Materials Science, University of Tokyo, Kashiwa, Chiba 277-8561, Japan*
[2]*SwissFEL, Paul Scherrer Institute, Forschungsstrasse 111, 5232 Villigen, Switzerland*
[3]*Department of Materials Science, Osaka Metropolitan University, Osaka 599-8531, Japan*
[4]*RIKEN SPring-8 Center, Sayo, Hyogo 679-5148, Japan*

Multiferroic CuO showing two distinct antiferromagnetic (AFM) phases: incommensurate (ICM) spiral and commensurate (CM) collinear AFM phases, is investigated by resonant x-ray diffraction (RXD) at the Cu L_3 edge. In the ICM phase where spin-spiral-induced ferroelectricity develops, circular dichroism ascribed to the handedness of the spiral magnetic order is observed at the magnetic Bragg (0.506, 0, −0.483) reflection. By measuring two-dimensional maps of the reflection intensity, the spatial distribution of the ferroelectric domains is clarified and is found to be strongly influenced by crystallographic twin structures. In the CM phase, weaker but substantial circular dichroic signals are observed at the magnetic Bragg (0.5, 0, −0.5) reflection. It is found that the spatial distributions of the circular dichroic signals resemble those in the ICM phase, suggesting some relation between the ICM and CM phases. The origin of the circular dichroic RXD observed in CuO is discussed based on the experimental observations.

I. INTRODUCTION

CuO (tenorite), known as a starting compound for high-T_C cuprate superconductors, has attracted considerable attention since its multiferroic nature was discovered [1]. The crystal structure of CuO is monoclinic (space group: $C2/c$), as illustrated in Fig. 1, which is unique among $3d$ transition-metal monoxides in departing from the simple NaCl-type structure [2]. This monoclinic structure is characterized by zigzag Cu-O chains along the [$10\bar{1}$] direction with the Cu-O-Cu bond angle of 146°. Partly related to such a structure involving moderate magnetic frustration, this compound exhibits successive antiferromagnetic (AFM) phase transitions at $T_{N1} = 213$ K and $T_{N2} = 230$ K [3–6]. At temperature (T) below T_{N1}, CuO shows a collinear AFM order, where the Cu moments point along the b axis with the commensurate (CM) propagation vector $\mathbf{q}_{CM}$ (0.5, 0, −0.5), as depicted in the right panel of Fig. 1 (CM phase). At $T_{N1} \leqslant T \leqslant T_{N2}$, the Cu moments show a spiral spin order with the incommensurate (ICM) propagation vector $\mathbf{q}_{ICM}$ (0.506, 0, −0.483), as depicted in the left panel of Fig. 1 (ICM phase). This spiral spin arrangement breaks inversion symmetry and induces improper ferroelectricity in which spin helicity is a primary order parameter [1]. Various theoretical approaches have been examined to clarify the mechanism of multiferroicity [7–10]. Owing to this multiferroic nature, the research on CuO has been extended to explore unique functionalities of the material, including electric-field control of chiral magnetic domains [11], optical control of magnetic order [12], and electric-field control of natural optical activity [13].

Apart from the multiferroic nature in the ICM phase, CuO has been proposed to have an orbital current in the CM phase [14]. The orbital current is characterized by a time-odd polar vector corresponding to an anapole or toroidal moment [15] and is proposed as the order parameter in the pseudogap phase of high-T_C cuprate superconductors [16,17] and the hidden ordered phase in $Sr_2(Ir, Rh)O_4$ [18]. Scagnoli *et al.* [14] performed a resonant x-ray diffraction (RXD) measurement at the Cu L_3 edge on CuO in the CM phase. They detected a nonzero σ'-σ polarization component in the magnetic Bragg (0.5, 0, −0.5) reflection, which is forbidden for resonant magnetic scattering with an electric dipole–electric dipole transition (E1-E1), usually the most relevant transition process in resonant scattering. Additionally, they observed that the intensity of the reflection strongly depends on the circular polarization of the incident beam, which should be absent for a collinear AFM order. Based on these observations, they claimed the possibility of an electric dipole–magnetic dipole (E1-M1) scattering from orbital currents around the copper atoms and resultant antiferroic order of anapole moments. However, orbital currents play no essential role in the interpretation of the observed circular dichroism on RXD in later theoretical studies. For example, Ref. [19] suggests that E1-M1 matrix elements must be too small to explain the experimental results, and Ref. [20] suggests that a birefringence effect explains the circular dichroism. Furthermore, Lovesey *et al.* [21,22] interpret the experimental data in terms of either an admixture of parity-even and parity-odd absorption events or a pure parity-even event with an allowance for absorption and birefringence. Thus, the existence of orbital currents in CuO is still under debate.

In principle, RXD using circularly polarized x rays is a powerful technique to examine the key order parameters in CuO, namely, spin helicity and anapole. The circular dichroic
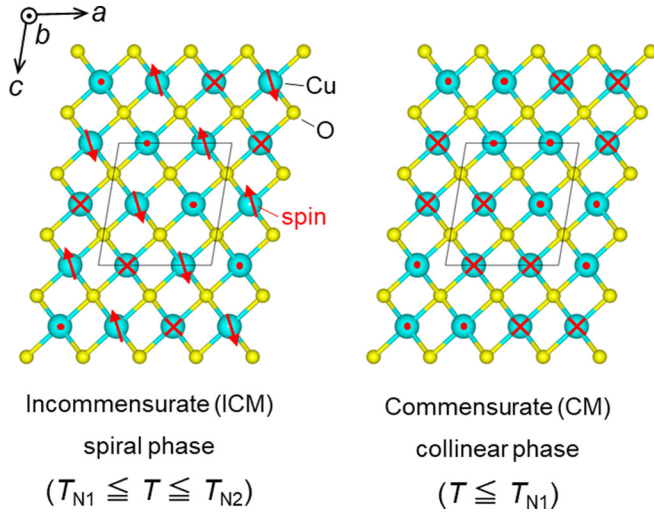
*misawa@crystal.k.u-tokyo.ac.jp

FIG. 1. Schematic drawings of magnetic structures in two antiferromagnetic (AFM) phases in CuO. (a) Incommensurate spiral AFM structure [$T_{N1}(= 213\,\text{K}) \leqslant T \leqslant T_{N2}(= 230\,\text{K})$] in which Cu spins (red arrows) rotate in a plane passing across the b axis with the propagation vector $\mathbf{q}_{\text{ICM}} = (0.506, 0, -0.483)$. (b) Commensurate collinear AFM structure ($T \leqslant T_{N1}$) with the propagation vector $\mathbf{q}_{\text{CM}} = (0.5, 0, -0.5)$ and Cu moments pointing along the b axis.

part in diffracted intensity couples to the sign of spin helicity or anapole. Furthermore, employing focused beams allows us to examine domain structures formed by these order parameters. Compared with the ICM phase where spin spiral order gives circular dichroism, domain observations in the CM phase are not trivial because of the discussed different interpretations. However, as the birefringence discussed in the CM phase [20] should not result in the spatial distribution of circular dichroism in RXD and the onset of the CM phase itself does not give distinct magnetic domains, observations of domains in the CM phase through the circular dichroism would support the anapole interpretation [14]. Here, to elucidate whether the anapole (or orbital current) interpretation is applicable to the circular dichroism of RXD in the CM phase of CuO, we investigate spatial distributions of circular dichroism on RXD in both the ICM and the CM phases of CuO by using circularly polarized focused x-ray beams with the energy around the Cu L_3 edge.

II. EXPERIMENT

Single crystals of CuO were grown from polycrystalline powder in a floating zone furnace equipped with two halogen lamps (Canon Machinery Inc.) under 8 atm of oxygen. The obtained crystals were oriented with Laue x-ray diffraction and cut into plate-shaped specimens with the widest faces parallel to the $(10\bar{1})$ plane. By using lapping papers with a minimum grain size of 0.1 μm, we mechanically polished the faces of two specimens (Samples #1 and #2) for RXD measurements.

Crystallographic defects such as twin structures of these samples were observed at room temperature by using a polarized light microscope and a transmission electron microscope (TEM). The TEM observation was performed by using a
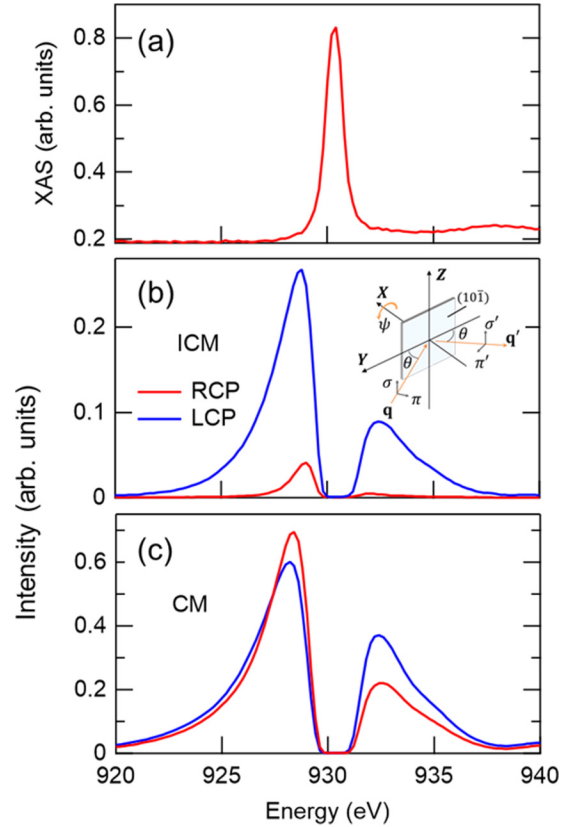

FIG. 2. Photon-energy profiles of x-ray absorption and magnetic Bragg reflections in the incommensurate (ICM) and commensurate (CM) antiferromagnetic phases near Cu L_3 edge. (a) X-ray absorption spectrum (XAS) obtained at 100 K. (b) Intensities of the (0.506, 0, −0.483) reflection at 220 K and (c) the (0.5, 0, −0.5) reflection at 140 K as a function of photon energy. Red and blue curves represent the data obtained with right and left circularly polarized incident x-rays. The inset shows the scattering geometry in which $\mathbf{q}$ ($\mathbf{q}'$) is the propagation vector of the incident (diffracted) x rays, and θ denotes the Bragg angle. The σ and σ' components are perpendicular to the scattering plane, and the π and π' components are parallel to the scattering plane.

JEM-2100F instrument at an acceleration voltage of 200 kV (JEOL Co. Ltd.). The sample area containing a twin running along the b axis was marked in a polarized-light-microscopy observation. The area was retrieved from a single crystal via a lift-out technique. A thin foil was fabricated by using a focused-ion-beam system (FB2200, Hitachi). The twin structures were analyzed by dark-field imaging and selected-area electron diffraction (ED). A Bragg reflection was strongly excited to obtain a dark-field image (two beam conditions).

RXD measurements were performed using an upgraded diffractometer based on the prototype instrument [23] at the beamline 17SU of SPring-8. Before RXD measurements, an x-ray absorption spectrum (XAS) was obtained. Figure 2(a) shows XAS measured at 100 K from a sample coated with sputtered Pt to observe the photo-induced electric current. A distinct peak structure is seen at ∼930 eV corresponding to the Cu L_3 absorption edge. For RXD measurements, the incident x-ray energy was set around the Cu L_3 absorption edge. The circular polarization of the incident

x rays at the energy used in the experiment is $|P_2| \geqslant 90\%$ in which P_2 is one of the Poincaré-Stokes parameters representing a polarization state. Here, $P_2 = +1(-1)$ corresponds to right (left) circular polarization [RCP (LCP)]. To observe magnetic Bragg reflections of $\mathbf{q}_{\mathrm{ICM}}$ for the ICM phase and $\mathbf{q}_{\mathrm{CM}}$ for the CM phase, Samples #1 and #2 were mounted with the $(10\bar{1})$ plane perpendicular to the scattering plane, which encompasses the propagation vectors $\mathbf{q}$ and $\mathbf{q}'$ of the incident and diffracted x rays, respectively. A schematic drawing of the diffraction geometry is illustrated in the inset of Fig. 2(b). The samples can be rotated along the scattering vectors $\mathbf{q}_{\mathrm{ICM}}$ and $\mathbf{q}_{\mathrm{CM}}$. This clockwise rotation is specified by the azimuthal angle ψ. The origin of $\psi = 0$ is defined as the geometry where the b axis is parallel to the scattering plane. A focused or unfocused incident x-ray beam can be chosen by changing the position of Kirkpatrick-Baez focusing mirrors located at 1 m before the sample position. The size of the focused beam is $\sim 30\ \mu$m in horizontal and 15 μm in vertical directions, and that of the unfocused beam is ~ 1 mm in horizontal and 0.8 mm in vertical directions. A Si photodiode is used to detect diffracted beams. For experiments using a focused beam, the diffraction intensity is normalized by the photo-induced current generated at the focusing mirror. For experiments using a nonfocused beam, the diffraction intensity is not normalized. In principle, normalization is unnecessary due to the high stability of SPring-8 ring current.

To observe spatial distributions of the diffracted intensity of the magnetic Bragg reflections, the specimens are positioned with an XYZ translation stage. The diffraction intensity itself significantly depends on the position of the samples due to the nonuniformity of the surface conditions and the crystallographic mosaicity of the samples. To eliminate these effects and extract the nature of circular dichroism from the data, we adopt the flipping ratio (FR) as a measure of circular dichroism, which is defined as FR $= \frac{I_{\mathrm{RCP}} - I_{\mathrm{LCP}}}{I_{\mathrm{RCP}} + I_{\mathrm{LCP}}}$, where I_{RCP} (I_{LCP}) denotes the integrated intensity of the magnetic reflections for RCP (LCP) incident x rays. For the analysis of mapping measurements, where the integral intensity cannot be calculated, FR$^{\circ} = \frac{I^{\circ}_{\mathrm{RCP}} - I^{\circ}_{\mathrm{LCP}}}{I^{\circ}_{\mathrm{RCP}} + I^{\circ}_{\mathrm{LCP}}}$, where I°_{RCP} (I°_{LCP}) denotes the intensity as it is was employed. In this paper, all data were taken in the absence of electric and magnetic fields after zero-field cooling.

III. RESULTS AND DISCUSSION

A. Comparison of circular dichroism in the ICM and CM phases

First, we measured the energy dependence of the magnetic Bragg reflections in the ICM and CM phases at certain positions of Sample #1 with the focused x-ray beam. Figures 2(b) and 2(c) show the energy profiles of the diffraction intensity of the reflections with $\mathbf{q}_{\mathrm{ICM}}$ at $T = 215$ K (ICM phase) and with $\mathbf{q}_{\mathrm{ICM}}$ at $T = 100$ K (CM phase), respectively. Red and blue lines denote the data obtained using RCP and LCP incident x rays, respectively. In both phases, the diffraction intensity shows resonant enhancement at the energies just below and above the Cu L_3 absorption edge (≈ 930 eV), while it is steeply suppressed at the energy of the edge due to the self-absorption effect. In the ICM phase, significant circular dichroism was

observed in the vicinity of the absorption edge [compare red and blue lines in Fig. 2(b)]. The circular dichroism on RXD for arbitrary spiral magnetic structures in various diffraction settings has been discussed by Zhang *et al.* [24]. The circular dichroism observed in the ICM phase is reasonably explained by applying their discussion to the ICM phase which has a tilted cycloidal spiral magnetic structure with the spin rotation plane at an angle of 73° with $\mathbf{q}_{\mathrm{ICM}}$ and 28° with the c axis [25]. The sign of circular dichroism does not flip between below and above the Cu L_3 edge, consistent with a single resonance (E1-E1).

The CM phase also shows substantial circular polarization dependence of the magnetic Bragg reflection, though the magnitude of the circular dichroism is weaker than that in the ICM phase [Fig. 2(c)]. Note that the beam irradiation position for the data in Fig. 2(c) is not the same as that in Fig. 2(b). Thus, the sign of the circular dichroism between these two phases cannot be compared with each other from these data. However, it is worth mentioning that the circular dichroism observed in the CM phase is opposite in sign at energies above and below the absorption edge, which is different from that observed in the ICM phase. This implies an occurrence of interference between two channels of resonant scattering in the CM phase, where their relative phase is reversed below and above the absorption edge. The feature is qualitatively consistent with the previous study [14], proposing an interference between the E1-M1 and E1-E1 transitions. On the other hand, the feature is against the interpretation based on birefringence [20] since the scattering is given only through an E1-E1 channel.

In the system showing spiral spin order, the sign of circular dichroism on RXD depends on that of the spin helicity [26,27]. This allows the visualization of spatial distributions of spin-helicity (handedness) domains (ferroelectric domains for spin-spiral multiferroics) by scanning a circularly polarized focused x-ray beam on the sample surface, which has been demonstrated in various spiral spin systems. [28–31]. Thus, in the multiferroic ICM phase of CuO, spin-helicity (or ferroelectric) domains can be visualized by measurements of scanning RXD using a circularly polarized focused x-ray beam. On the other hand, in the CM phase, if we adopt the interpretation in Ref. [14], the sign of the circular dichroism on RXD depends on that of the anapole moment. This means that anapole domains can be visualized through the circular dichroism, whereas birefringence is uniform throughout a sample if staying on crystallographically equivalent domains. To examine these domain structures, we investigate spatial distributions of circular dichroism on RXD in both ICM and CM phases by scanning a circularly polarized focused x-ray beam on the sample surface.

Figure 3 shows two-dimensional maps of FR$^{\circ}$ observed on the face parallel to $(10\bar{1})$ of Sample #1 in the ICM and the CM phases. Figures 3(a) and 3(c) were obtained using the reflection with $\mathbf{q}_{\mathrm{ICM}}$ at $T = 215$ K (ICM phase), while Figs. 3(b) and 3(d) were taken using that with $\mathbf{q}_{\mathrm{ICM}}$ at $T = 100$ K (CM phase). All the maps were taken at the azimuthal angle $\psi = 90°$ (the b axis is perpendicular to the scattering plane) using incident x rays with the energy of 928.9 eV. First, the maps of Figs. 3(a) and 3(b) were obtained in a series of measurements without heating the sample above T_{N2}. Clear
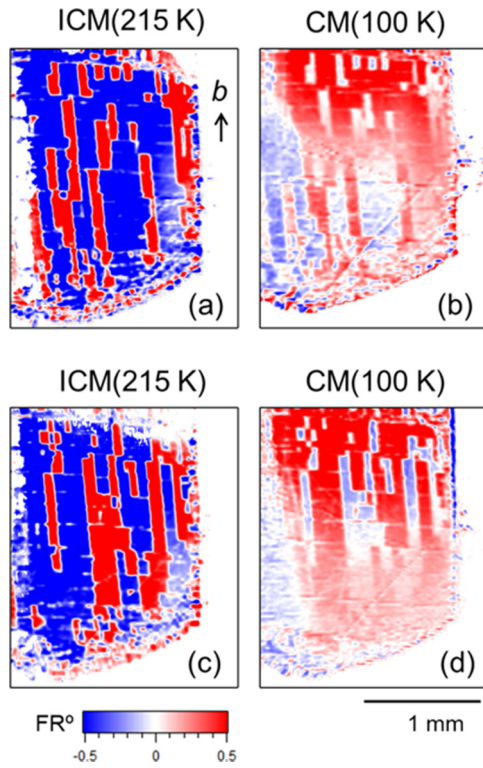
FIG. 3. Two-dimensional maps of the flipping ratio of magnetic Bragg reflections in the incommensurate (ICM) and commensurate (CM) antiferromagnetic phases of a CuO crystal with the widest face parallel to the $(10\bar{1})$ plane (Sample #1). (a) and (c) Those of the $(0.506, 0, -0.483)$ reflection in the ICM phase at 215 K. (b) and (d) Those of the $(0.5, 0, -0.5)$ reflection in the CM phase at 100 K. Scale bar: 1 mm. The measurements have been done at the azimuthal angle $\psi = 90°$. The upper maps [(a) and (b)] were obtained in a series of measurements without heating the crystal above T_{N2} ($= 230$ K). After the measurements of (a) and (b), the crystal was heated to a temperature above T_{N2} and then cooled. Subsequently, the maps of (c) and (d) were obtained.

color contrast is seen in the map of the ICM phase [Fig. 3(a)], which corresponds to spin-helicity (and ferroelectric) domain structures, as observed in several spin-spiral multiferroics [29,30]. A characteristic feature of the domain pattern is that most domain boundaries are formed in a straight manner and elongated along the b axis. At $T = 100$ K in the CM phase, weaker but substantial color contrast is still seen [Fig. 3(b)], which suggests the presence of a certain type of domain. It is worth mentioning that the positions of domain boundaries are the same as those in the ICM phase within the experimental precision [compare Figs. 3(a) and 3(b)]. In addition, the FR° signs of the upper area shown in Fig. 3(b) are opposite to those observed in Fig. 3(a), while those of the lower area in Fig. 3(b) seem to be the same as those in Fig. 3(a). This suggests that the signs of FR° in the two phases are not correlated. After taking the maps of Figs. 3(a) and 3(b), the sample was heated to a temperature above T_{N2} and then cooled. Subsequently, the maps of Figs. 3(c) and 3(d) were obtained. Comparing Figs. 3(b) and 3(d) with Figs. 3(a) and 3(c), essential features of the domain patterns: line-shaped domain boundaries and correlation of the boundary positions between the two phases,
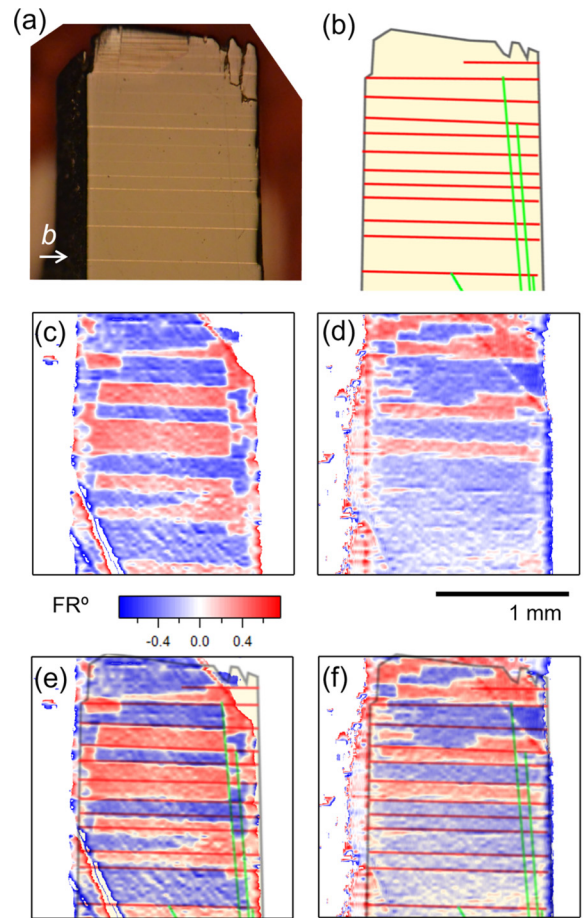

FIG. 4. Comparison between crystallographic twin structures and spatial distributions of the flipping ratio (FR) of the $(0.5, 0, -0.5)$ reflection in the commensurate (CM) phase. (a) A polarized-light microscopy image of Sample #2 used for the resonant x-ray diffraction (RXD) measurements (Sample #2). The widest face of the crystal is parallel to the $(10\bar{1})$ plane. Dark areas and bright line-shaped areas are crystallographic twins. (b) A sketch of (a). Red and green lines represent the positions of the bright and dark line-shaped areas, respectively. (c) and (d) Two-dimensional maps of the FR of the $(0.5, 0, -0.5)$ reflection in the CM phase at 100 K. The measurements have been done at the azimuthal angle $\psi = 0°$. Scale bar: 1 mm. After the measurements of (c), the crystal was heated to a temperature above T_{N2} and then cooled to 100 K. Subsequently, the map of (d) was obtained. (e) and (f) Images of direct overlap of (b) with (c) and (d).

are well reproduced. However, the domain pattern changes once the sample is heated to a temperature above T_{N2}. This suggests that the domains observed in both ICM and CM phases are ascribed to a magnetic origin and are correlated with each other.

B. Correlation between magnetic domains and crystallographic twin domains

As shown in Fig. 3, rectilinear domain boundaries were observed in both CM and ICM phases. Here, we examine the correlation between the crystallographic defects and the domain boundaries. In fact, CuO with the $C2/c$ monoclinic structure is subject to the formation of twin domains [32–34].
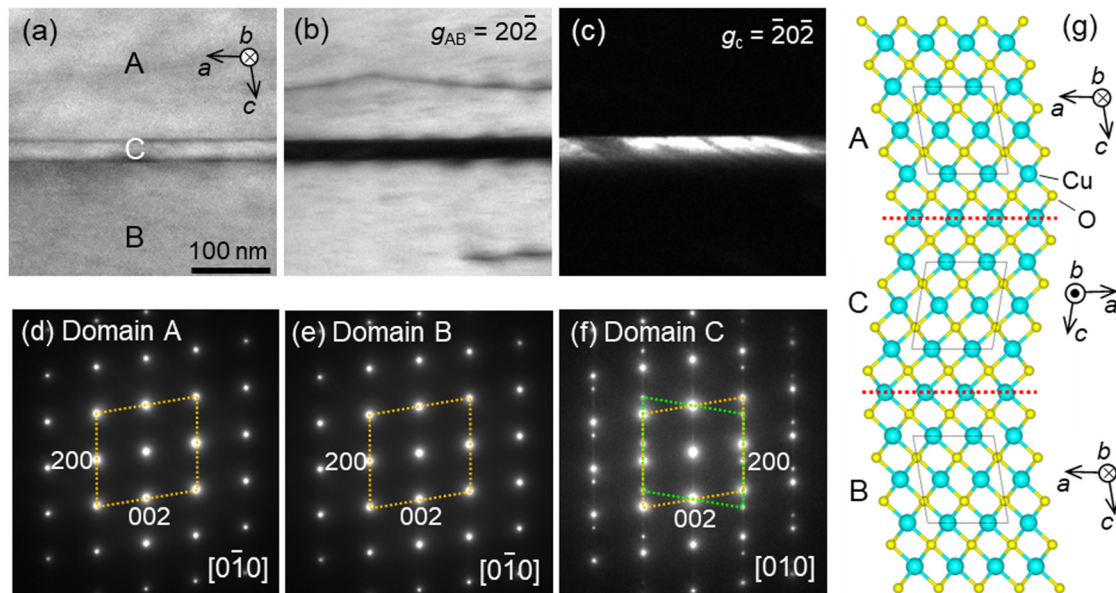
FIG. 5. A twin structure observed by dark-field imaging and selected-area electron diffraction (ED). (a) A bright-field image in an area with two twin boundaries. The corresponding dark-field images using reflections (b) $20\bar{2}$ and (c) $\bar{2}0\bar{2}$. ED patterns for the [$0\bar{1}0$] (or [010]) incidence around the regions (d) A, (e) B, and (f) C in (a). Note that the reflections from both twin domains are shown in (f). (g) A twin structure whose boundaries are parallel to the (001) plane, which explains the experimental observation.

Figure 4(a) is a polarized-light microscopy image of the face parallel to ($10\bar{1}$) of Sample #2 at room temperature. Many bright lines parallel to the b axis and some dark lines along different directions are seen, which are schematically illustrated as red and green lines, respectively, in Fig. 4(b). The contrast seen in the polarized-light microscopy image reflects the presence of crystallographic defects such as twin domains, which is discussed later based on ED patterns. Figures 4(c) and 4(d) display spatial distributions of FR° for the (0.5, 0, −0.5) reflection at the area corresponding to that in Fig. 4(a). These maps were taken at $\psi = 0°$ (the b axis is parallel to the scattering plane). First, the map shown in Fig. 4(c) was obtained at 100 K (CM phase). Subsequently, once the sample was heated up to room temperature, then the map shown in Fig. 4(d) was obtained at 100 K again. It is found that the texture of FR° has rectilinear domain boundaries mostly along the b axis and drastically changes once the sample undergoes a transition into the paramagnetic phase, which is essentially the same as the results of Sample #1 [Fig. 3]. Importantly, the rectilinear domain boundaries in the FR maps locate on the positions of the bright or dark lines in the polarized-light microscopy image [Fig. 4(a)]. This is clearly seen in the images of direct overlap of Fig. 4(b) with Figs. 4(c) and 4(d), which is shown in Figs. 4(e) and 4(f). This correlation suggests that the domain boundaries observed in circular dichroism on RXD are strongly clamped by the crystallographic defects. However, the change in domain patterns [compare Figs. 4(c) and 4(d)] implies that the circular dichroism is not simply due to the crystallographic origin such as birefringence [19] but due to the magnetic order itself and/or another order developing in association with the magnetic order.

To clarify the origin of the line-shaped domain boundaries observed in Fig. 4, ED observations were performed. Figure 5(a) shows a bright-field image viewed along the b axis of a CuO crystal. A line-shaped structure is clearly seen and forms three domains A, B, and C. Dark-field images [Figs. 5(b) and 5(c)] and ED patterns [Figs. 5(d)–5(f)] were captured in these domains to reveal their microstructures. As seen in Figs. 5(d) and 5(e), domains A and B exhibit the same ED patterns, demonstrating the same crystallographic orientation in these domains. The inset of Fig. 5(a) depicts the crystallographic orientation in domains A and B. The boundary plane is parallel to both a and b axes. Conversely, the ED pattern from domain C [Fig. 5(f)] exhibits the symmetry rotated about the c^* axis by 180° in domain A (green dotted box): The 002 reflections from the two domains are in the same place, and the 200 reflections are the other way around. Note that the observation area of our ED patterns is $>100 \times 100$ nm^2, and thus, the measurement around domain C with a width of ~30 nm contains reflections from both domains C and A (or B). Thus, the crystallographic orientation in domain C is related by the 180° rotation about the c^* axis of that in A (or B), demonstrating the presence of a twin domain. The dark-field images using reflections $20\bar{2}$ [Fig. 5(b)] and $\bar{2}0\bar{2}$ [Fig. 5(c)] at the same region of Fig. 5(a) also support this twin domain. The real-space observation suggests that the crystallographic axes are equivalent in domains A and B because the domains are bright similarly. Additionally, the bright domain C of Fig. 5(c) causes the green-marked reflections because the dark-field image used reflection $\bar{2}0\bar{2}$ of the twin. The results can be summarized in the twin structure model illustrated in Fig. 5(g), in which the twin boundaries are parallel to the (001) plane. The (001) plane of the boundary agrees with the line that runs along the b axis in Fig. 4. This indicates that the domain structures observed in RXD measurements are strongly coupled with crystallographic twin structures.

C. Azimuthal angle dependence of circular dichroism in the CM phase

The azimuthal angle dependence of the circular dichroism is important for comparison between experimental results and theoretical analysis as discussed in the literature [14,20]. Two-dimensional maps shown in Figs. 3 and 4 suggest that the circular dichroism depends on domains, requiring a careful investigation of the scale of the domain size for the discussion. We examined circular dichroism at various azimuthal angles with the use of both unfocused and focused x-ray beams. RXD profiles using an unfocused beam have been taken from Sample #2 at 100 K to look at averaged signals. The results measured at three different azimuthal angles are shown in Figs. 6(a)–6(f). The profiles shown in Figs. 6(a)–6(c) and Figs. 6(d)–6(f) were taken at the x-ray energies of 929.2 and 932.0 eV, respectively, corresponding to the peak positions seen in the energy profile of the diffraction intensity [see Fig. 2(c)]. At $\psi = 50°$, remarkable circular dichroism is observed, and its sign is reversed between 929.2 eV [Fig. 6(a)] and 932.0 eV [Fig. 6(d)]. With increasing ψ, the circular dichroism is gradually suppressed and vanishes at $\psi = 90°$ [Figs. 6(c) and 6(f)]. Figure 6(g) plots the ψ dependence of $\Delta I = I_{RCP} - I_{LCP}$ measured at the two energies. Here, I_{RCP} and I_{LCP} are the integrated intensities of the diffraction profile at each ψ. A clear sign reversal is seen between the data at 929.2 and 932.0 eV. Each curve is well fitted by the equation derived from the discussion based on the interference of the E1-M1 and E1-E1 transitions in which ΔI is proportional to $\sin 2\psi$ [14]. Thus, the results obtained by the unfocused beam reproduce well the previous results that suggest circular dichroism in anapole (or orbital current) origin [14]. Note that, considering the typical domain size found in the two-dimensional maps in Fig. 4, the area irradiated by the unfocused beam probably has multiple domains, meaning that we measure averaged signals of the domains.

To clarify the azimuthal-angle dependence of circular dichroism within a single domain, two-dimensional FR maps were measured at various azimuthal angles with the use of the focused x-ray beam. The results at various ψ are shown in Figs. 7(a)–7(g). The maps were obtained at 929.2 eV by sequential measurements with keeping the temperature at 100 K. As ψ is changed, the contrast changes while maintaining the circular dichroic texture. To compare the results obtained with the unfocused beam shown in Fig. 6(g), the ψ dependence of average FR in each map is plotted in Fig. 7(h) together with that obtained using the unfocused beam shown in Fig 6(g). These two sets of data are well accorded with each other [compare filled circles and open triangles in Fig. 7(h)]. This is reasonable because both datasets reflect average diffraction intensities from the sample surface. By contrast, the ψ dependence of diffraction intensity in each domain shows different behavior. The FR data at positions A and B in Fig. 7(a) are also plotted in Fig. 7(h). Specifically, FR at A (B) appears to be vertically shifted in the positive (negative) direction. As a result, a finite contrast remains even at $\psi = 0°$ and $90°$, where RXD has no circular dichroism in the previous studies [14,20].
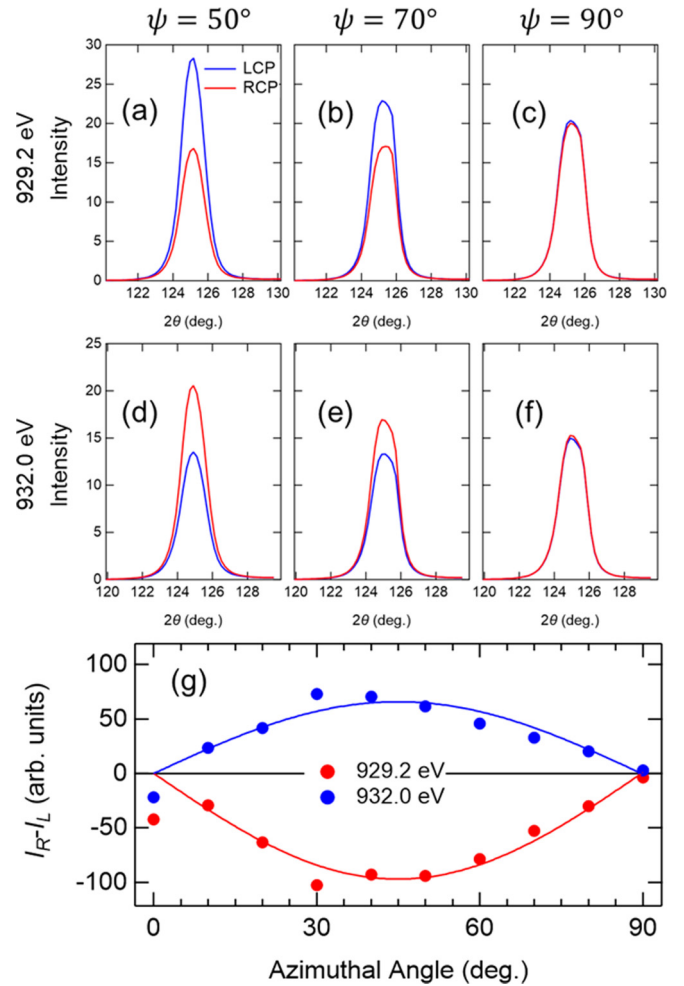

FIG. 6. Azimuthal angle dependence of circular dichroism of resonant x-ray diffraction (RXD) measured with unfocused x-ray beams in the commensurate phase at 100 K. (a)–(f) Comparison of the θ-2θ scans around the (0.5, 0, −0.5) reflection obtained at selected azimuthal angles with left circularly polarized (LCP) and right circularly polarized (RCP) incident x rays. The data of (a)–(c) and (d)–(f) were taken at photon energies of 929.2 and 932.0 eV, respectively. (g) Azimuthal-angle dependence of the difference between the (0.5, 0, −0.5) reflection obtained with LCP and RCP incident x rays. The blue and red points represent the data obtained at 929.2 and 932.0 eV. These data were obtained by using the unfocused x-ray beam.

At the present stage, we do not have a clear explanation for the ψ dependence of circular dichroism observed within each domain. However, the similarity of domain patterns observed in the ICM and CM phases suggests that the order parameters of these two phases are correlated. In CuO, an anomalous memory effect for the direction of the ferroelectric polarization, coupled to spin helicity, is observed in the transition from the paraelectric CM phase to the ferroelectric ICM phase and is explained in terms of the existence of multiferroic nanoregions preserving spin helicity in the CM phase [35]. Thus, though the correlation between the ICM and CM phases can be anticipated in the two magnetic phases, there is likely a direct coupling between the order parameters not as a residual minor phase.
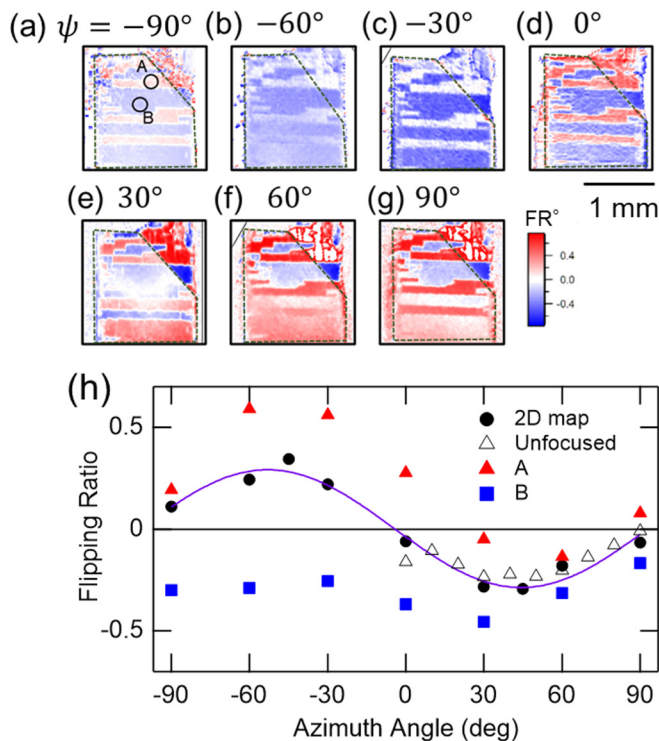
FIG. 7. Azimuthal-angle dependence of circular dichroism of resonant x-ray diffraction (RXD) measured with the focused x-ray beam in the commensurate (CM) phase at 100 K. The data were obtained for Sample #2 at 929.2 eV. (a)–(g) Two-dimensional maps of the $(0.5, 0, -0.5)$ reflection at various azimuthal angles. The area of uniform sample surface is surrounded by as a dashed line in each panel. Scale bar: 1 mm. (h) Azimuthal-angle dependence of the flipping ratio between the $(0.5, 0, -0.5)$ reflection obtained with right circularly polarized (RCP) and left circularly polarized (LCP) incident x rays. Black closed circles denote the data obtained by the average of each two-dimensional map in (a)–(g). Red triangles and blue squares denote the data taken at positions A and B, respectively, in (a). For comparison, the data obtained by the unfocused beam shown in Fig. 6 are also plotted (black open triangles).

IV. SUMMARY

Circular dichroism of RXD was investigated in the ICM spiral AFM phase and the CM collinear AFM phase of mul-tiferroic CuO. In both phases, substantial circular dichroism was observed for their magnetic Bragg reflections. In the ICM phase where spin-spiral-induced ferroelectricity develops, it is reasonably considered that circular dichroism and its sign are ascribed to the spiral magnetic order and the sign of spin helicity (i.e., ferroelectricity), respectively. In the CM phase, weaker but substantial circular dichroic signals are observed. Measurements of spatial distributions of the circular dichroism revealed the presence of magnetic domains with rectilinear domain boundaries in both phases. It is found that the domain structures in the two phases resemble each other, suggesting some correlation between the ICM and CM phases. Furthermore, comparison of the magnetic domain structures with dark-field images obtained by ED measurements revealed that the domain boundaries observed in the two phases are strongly influenced by crystallographic twin structures. The azimuthal angle dependence of the circular dichroism in the CM phase using unfocused x-ray beams is essentially consistent with the previous study in which the circular dichroism is explained in terms of the anapole (or orbital current) interpretation via the interference of the E1-M1 and E1-E1 transitions. However, the result of local measurements within each domain is not fully explained by the conventional discussions. Thus, more comprehensive discussions are required to understand the origin of the circular dichroism in the CM phase of CuO.

[1] T. Kimura, Y. Sekio, H. Nakamura, T. Siegrist, and A. P. Ramirez, Nat. Mater. **7**, 291 (2008).

[2] S. Åsbrink and L.-J. Norrby, Acta Crystallogr. B **26**, 8 (1970).

[3] B. X. Yang, T. R. Thurston, J. M. Tranquada, and G. Shirane, Phys. Rev. B **39**, 4343 (1989).

[4] J. B. Forsyth, P. J. Brown, and B. M. Wanklyn, J. Phys. C **21**, 2917 (1989).

[5] M. Ain, A. Menelle, B. M. Wanklyn, and E. F. Bertaut, J. Phys. Condens. Matter **4**, 5327 (1992).

[6] N. Qureshi, E. Ressouche, A. Mukhin, M. Gospodinov, and V. Skumryev, Sci. Adv. **6**, eaay7661 (2020).

[7] G. Giovannetti, S. Kumar, A. Stroppa, J. van den Brink, S. Picozzi, and J. Lorenzana, Phys. Rev. Lett. **106**, 026401 (2011).

[8] P. Toledano, N. Leo, D. D. Khalyavin, L. C. Chapon, T. Hoffmann, D. Meier, and M. Fiebig, Phys. Rev. Lett. **106**, 257601 (2011).

[9] G. Jin, K. Cao, G.-C. Guo, and L. He, Phys. Rev. Lett. **108**, 187205 (2012).

[10] X. Rocquefelte, K. Schwarz, P. Blaha, S. Kumar, and J. van den Brink, Nat. Commun. **4**, 2511 (2013).

[11] P. Babkevich, A. Poole, R. D. Johnson, B. Roessli, D. Prabhakaran, and A. T. Boothroyd, Phys. Rev. B **85**, 134428 (2012).

[12] S. L. Johnson, R. A. de Souza, U. Staub, P. Beaud, E. Möhr-Vorobeva, G. Ingold, A. Caviezel, V. Scagnoli, W. F. Schlotter, J. J. Turner *et al.*, Phys. Rev. Lett. **108**, 037203 (2012).

[13] R. Masuda, Y. Kaneko, Y. Tokura, and Y. Takahashi, Science **372**, 496 (2021).

[14] V. Scagnoli, U. Staub, Y. Bodenthin, R. A. de Souza, M. García-Fernández, M. Garganourakis, A. T. Boothroyd, D. Prabhakaran, and S. W. Lovesey, Science **332**, 696 (2011).

[15] P. Bourges, D. Bounoua, and Y. Sidis, C.R. Phys. **22**, 7 (2021).

[16] M. E. Simon and C. M. Varma, Phys. Rev. Lett. **89**, 247003 (2002).

[17] C. M. Varma, Phys. Rev. B **73**, 155113 (2006).

[18] J. Jeong, Y. Sidis, A. Louat, V. Brouet, and P. Bourges, Nat. Commun. **8**, 15119 (2017).

[19] S. Di Matteo and M. R. Norman, Phys. Rev. B **85**, 235143 (2012).

[20] Y. Joly, S. P. Collins, S. Grenier, H. C. N. Tolentino, and M. De Santis, Phys. Rev. B **86**, 220101(R) (2012).

[21] S. W. Lovesey and E. Balcar, J. Phys. Soc. Jpn. **82**, 021008 (2013).

[22] S. W. Lovesey, V. Scagnoli, A. N. Dobrynin, Y. Joly, and S. P. Collins, J. Phys.: Condens. Matter **26**, 125504 (2014).

[23] T. Takeuchi, A. Chainani, Y. Takata, Y. Tanaka, M. Oura, M. Tsubota, Y. Senba, H. Ohashi, T. Mochiku, K. Hirata *et al.*, Rev. Sci. Instrum. **80**, 023905 (2009).

[24] S. L. Zhang, G. van der Laan, and T. Hesjedal, Phys. Rev. B **96**, 094401 (2017).

[25] P. J. Brown, T. Chattopadhyay, J. B. Forsyth, and V. Nunez, J. Phys. Condens. Matter **3**, 4281 (1991).

[26] J. P. Hill and D. F. McMorrow, Acta Cryst. A **52**, 236 (1996).

[27] P. G. Evans and E. D. Isaacs, J. Phys.: D Appl. Phys. **39**, R245 (2006).

[28] J. C. Lang, D. R. Lee, D. Haskel, and G. Srajer, J. Appl. Phys. **95**, 6537 (2004).

[29] E. Schierle, V. Soltwisch, D. Schmitz, R. Feyerherm, A. Maljuk, F. Yokaichiya, D. N. Argyriou, and E. Weschke, Phys. Rev. Lett. **105**, 167207 (2010).

[30] Y. Hiraoka, Y. Tanaka, T. Kojima, Y. Takata, M. Oura, Y. Senba, H. Ohashi, Y. Wakabayashi, S. Shin, and T. Kimura, Phys. Rev. B **84**, 064418 (2011).

[31] H. Ohsumi, A. Tokuda, S. Takeshita, M. Takata, M. Suzuki, N. Kawamura, Y. Kousaka, J. Akimitsu, and T.-h. Arima, Angew. Chem. Int. Ed. **52**, 8718 (2013).

[32] G. N. Kryukova, V. I. Zaikovskii, V. A. Sadykov, S. F. Tikhov, V. V. Popovskii, and N. N. Bulgakov, J. Solid State Chem. **73**, 191 (1988).

[33] A. A. Bush, V. Ya. Shkuratov, A. B. Kuz'menko, and E. A. Tishchenko, Crystallogr. Rep. **47**, 335 (2002).

[34] H. Sheng, H. Zheng, S. Jia, L. Li, F. Cao, S. Wu, W. Han, H. Liu, D. Zhao, and J. Wang, J. Appl. Cryst. **49**, 462 (2016).

[35] W. B. Wu, D. J. Huang, J. Okamoto, S. W. Huang, Y. Sekio, T. Kimura, and C. T. Chen, Phys. Rev. B **81**, 172409 (2010).

[36] K. Momma and F. Izumi, J. Appl. Cryst. **44**, 1272 (2011).